ACS APPLIED NANO MATERIALS

www.acsanm.org

Article

In Situ Monitoring of Scale Effects on Phase Selection and Plasmonic Shifts during the Growth of AgCu Alloy Nanostructures for Anticounterfeiting Applications

Matthias Schwartzkopf, André Rothkirch, Niko Carstens, Qing Chen, Thomas Strunskus, Franziska C. Löhrer, Senlin Xia, Christoph Rosemann, Lorenz Bießmann, Volker Körstgens, Shiwani Ahuja, Pallavi Pandit, Jan Rubeck, Susann Frenzke, Alexander Hinz, Oleksandr Polonskyi, Peter Müller-Buschbaum, Franz Faupel, and Stephan V. Roth*

Cite This: *ACS Appl. Nano Mater.* 2022, 5, 3832−3842

Read Online

ACCESS | Metrics & More | Article Recommendations | Supporting Information

ABSTRACT: Tailoring of plasmon resonances is essential for applications in anticounterfeiting. This is readily achieved by tuning the composition of alloyed metal clusters; in the simplest case, binary alloys are used. Yet, one challenge is the correlation of cluster morphology and composition with the changing optoelectronic properties. Hitherto, the early stages of metal alloy nanocluster formation in immiscible binary systems such as silver and copper have been accessible by molecular dynamics (MD) simulations and transmission electron microscopy (TEM). Here, we investigate in real time the formation of supported silver, copper, and silver−copper-alloy nanoclusters during sputter deposition on poly(methyl methacrylate) by combining in situ surface-sensitive X-ray scattering with optical spectroscopy. While following the transient growth morphologies, we quantify the early stages of phase separation at the nanoscale, follow the shifts of surface plasmon resonances, and quantify the growth kinetics of the nanogranular layers at different thresholds. We are able to extract the influence of scaling effects on the nucleation and phase selection. The internal structure of the alloy cluster shows a copper-rich core/silver-rich shell structure because the copper core yields a lower mobility and higher crystallization tendency than the silver fraction. We compare our results to MD simulation and TEM data. This demonstrates a route to tailor accurately the plasmon resonances of nanosized, polymer-supported clusters which is a crucial prerequisite for anticounterfeiting.

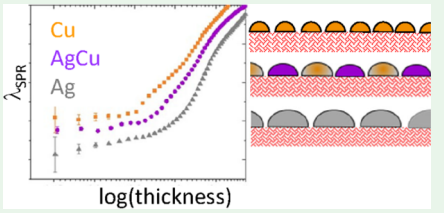

KEYWORDS: *plasmon resonance, percolation, growth kinetics, GISAXS, GIWAXS*

INTRODUCTION

The tuning of plasmon resonances has important applications in biosensor devices[1−5] and photovoltaics[6,7] because the plasmon resonance strongly depends on the cluster size, arrangement, the materials used, and their composition.[8] Especially the use of bimetallic alloys allows for fine-tuning of the plasmon resonance,[9] which offers new pathways in anticounterfeiting: in combination with polymer supports and templates,[10] structural color can readily be achieved by exploiting the plasmon resonance.[4,11−13] Moreover, this enables fast electrochromic color switching of smart windows.[14] Hence, understanding the correlation of size and composition with the plasmonic and optoelectronic behavior of polymer-supported metal cluster systems carries high potential but also is a challenge. The kinetics of the formation of single-component clusters on surfaces and their physical properties has extensively been investigated, both by theory and experiments.[10,15−18] Besides such single-component clusters, presently alloys or multicomponent-supported clusters receive increasing attention. Prominent supported cluster synthesis methods include chemical methods[19] and vacuum deposition.[20−22] Hence, already much effort has been undertaken to synthesize such multicomponent and metallic clusters using different methods such as pyrolysis,[23] sol−gel synthesis,[24] templating,[25] aggregation sources,[26,27] and sputter deposition.[8,28,29] The nucleation and growth of silver and copper clusters during magnetron sputtering was observed very successfully by X-ray scattering.[30,31] Applications of supported clusters range from heterogeneous catalysis[32] and photocatalysis[33] to information technology[34] and solar cells[35] as well as anticounterfeiting.[36−39] Here, nanoscale heterostructures and alloying allow for the facile tuning of chemical and optoelectronic properties.[40,41] Sputter deposition allows for alloying and high cluster density layers,[42] enabling, for

Received: December 23, 2021
Accepted: February 9, 2022
Published: February 25, 2022

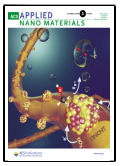

example, an organic shell-free cluster incorporated in layer-by-layer printing processes.[43]

In this respect, the kinetics during the formation of bimetallic clusters has attracted big interest. Especially the temporal evolution of their electronic and geometric structure was investigated.[44,45] Observing the formation of such bimetallic clusters during deposition and the concomitant phase separation on the nanoscale in real-time was hitherto accessed by molecular dynamics (MD) simulations.[46] In detail, the system silver (Ag)−copper (Cu) alloy has received considerable attraction. In AgCu clusters, a strong tendency of Ag and Cu to demix is observed. Ag is predicted to segregate at the surface. This can even lead to a wetting of Ag on the Cu core.[47] Hence, we focus in the present study on this interesting alloy system.

Here, we present a combined in situ study using grazing-incidence small- and wide-angle X-ray scattering (GISAXS/GIWAXS) and UV−vis spectroscopy during sputter deposition to observe in real-time and quantitatively the alloy cluster formation and phase separation of the immiscible Ag−Cu binary system during growth on poly(methyl methacrylate) (PMMA) thin films. The onset of phase separation is identified and correlated with the occurrence and red-shift of the plasmon resonance, which can be taken as a fingerprint for future large-scale manufacturing because UV−vis spectroscopy is a well-established industry process. We complement our results by high-resolution transmission electron microscopy (HRTEM) to corroborate the demixing stage and atomic force microscopy (AFM) to probe the differences in metal cluster morphology and percolation. We are able to deduce mobility coefficients for Ag, Cu, and $Ag_{42}Cu_{58}$ alloy clusters. TEM is a well-established method for investigating Cu−Ag nanoalloy structures.[48−50] Our results show quantitative agreement with MD simulations from Bonitz et al.[46] Based on the knowledge on the nanoscale dynamics, the plasmon resonance shift induced by morphological changes is quantified, which makes it useful for anticounterfeiting based on nanoscale heterostructures.[12,51]

EXPERIMENTAL SECTION

Materials. Thin PMMA films were spin-coated with a thickness of (80 ± 5) nm. PMMA has a M_w = 267 kg/mol and a polydispersity of P = 1.3 (Polymer Source Inc., Canada). The polymer films were deposited by spin coating using polymer solution in toluene (12.5 g/L) onto acid pre-cleaned Si(100) substrates (size 12 × 15 mm^2, Si-Mat). The spin coater used was Delta 10TT (SÜSS Micro Tec Lithography, Germany, 850 rpm, ramp 9, 30 s).

For sputter deposition, targets were 2 inch in diameter, obtained from Kurt J. Lesker with purity > 99.99.%. Targets were Ag, Cu, and Ag−Cu with a ratio of 42.4:57.6 for the alloy target. We refer to the composition as 42:58 (Ag−Cu).

Sputter Deposition. Sputter deposition was performed using a custom-built direct current (DC) magnetron sputter chamber, described in earlier experiments.[52] Sputter deposition is a mature physical vapor deposition technology with reliable repeatability.[16,53,54] We adjusted the deposition rates (J = 0.15 ± 0.01 nm/s) to be as similar as possible using a quartz crystal microbalance. However, in this deposition regime, we expect no significant change in the percolation threshold based on the deposition rate.[53] For alloy cluster deposition, we used a single alloy target, see above. The sputter deposition parameters are summarized in Table S1, Supporting Information. Scheme 1 illustrates the bottom-up multilayer system and fabrication from a material perspective (spin coating of PMMA from toluene and subsequent sputter deposition of Cu, Ag, and the alloy). This functional stack consisting of metal alloy clusters/PMMA spacer layer/silicon as mirror substrate exactly follows the layout used for anticounterfeiting outlined by Walter et al.[55] and Dobrowolski et al.[39]

Scheme 1. In the First Step, PMMA is Spin-Coated from Toluene Solution onto a Cleaned Silicon (Si) Wafer and is Dried under Ambient Conditions; the Fabricated PMMA Spacer Layer of 80 nm Thickness on Si is Transferred to the Sputter Deposition Chamber; Cu (x = 0), Ag (x = 1), and the Alloy (x = 0.42) are Deposited onto the Thin PMMA Film via DC Magnetron Sputter Deposition

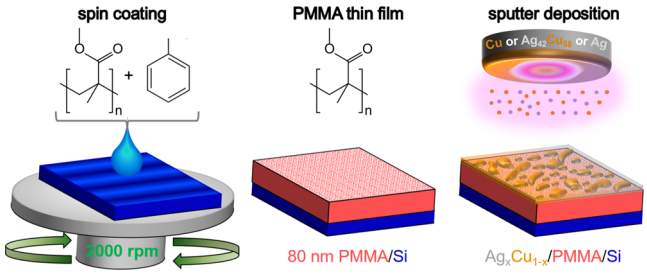

Atomic Force Microscopy. AFM measurements were performed using the tapping mode (NTEGRA Probe Nano-Laboratory, Russia). High-resolution NSG03 semi-contact cantilevers with a tip radius of 6 nm and a resonant frequency of (90 ± 8) kHz (NT-MDT, Russia) were used to measure AFM. For each sample, AFM images were taken with scan sizes of 6 × 6 μm^2, 2 × 2 μm^2, and 1 × 1 μm^2.

Transmission Electron Microscopy. TEM was performed using a Jeol JEM-2100 (Tokyo, Japan). The acceleration voltage was set to 200 kV using a LaB_6 cathode. For TEM sample preparation in this work, the alloy films were deposited on carbon-coated copper grids.

Grazing-Incidence Small- and Wide-Angle X-ray Scattering. The details of the in situ GISAXS/GIWAXS experiments combined with sputter deposition as well as the details of the analysis are given in the Supporting Information. Due to the enlarged footprint in GISAXS and GIWAXS, statistical relevant morphology and structure data are retrieved.

Surface Differential Reflection Spectroscopy. A deuterium halogen source (Ocean Insight, DH-2000-BAL), providing UV−vis−NIR light, and a detector (Ocean Insight, STS-Vis) with a spectral range from 340 to 820 nm were used. Both light source and detector were assembled to viewports at the process chamber under an angle of incidence of 55°. Because the reflection UV−vis experiments were performed in situ, the sample was not exposed to air during these measurements. Therefore, oxidation was ruled out. This is advantageous for experiments involving Cu and CuAg in particular because Cu is prone to oxidation (especially for nanoscale clusters due to their high surface/volume ratio).

RESULTS AND DISCUSSION

We present here the results of the combined time-resolved GISAXS/GIWAXS and in situ sputter deposition experiments on the three investigated systems on PMMA: Ag, Cu, and $Ag_{42}Cu_{58}$. The analysis of the GIWAXS data provides in situ information on the phase separation in the crystalline parts of the clusters. Figure 1a−c shows the one-dimensional cake-cuts of the 2D GIWAXS data $I(2\theta)$ with θ being the diffraction angle for Ag, Cu, and $Ag_{42}Cu_{58}$ alloy (nominal alloy composition). Data are shown at five selected deposited effective thicknesses together with the corresponding fits based on Lorentzian functions for extracting peak positions, amplitudes, and widths. Details of the analysis are given in the Supporting Information. In the case of Ag, the Ag(111) peak has a much higher intensity than the Ag(200) peak (Figure 1a). In the case of Cu, only the Cu(111) peak is visible given that the Cu(200) peak is located outside the 2θ range

https://doi.org/10.1021/acsanm.1c04473
ACS Appl. Nano Mater. 2022, 5, 3832−3842

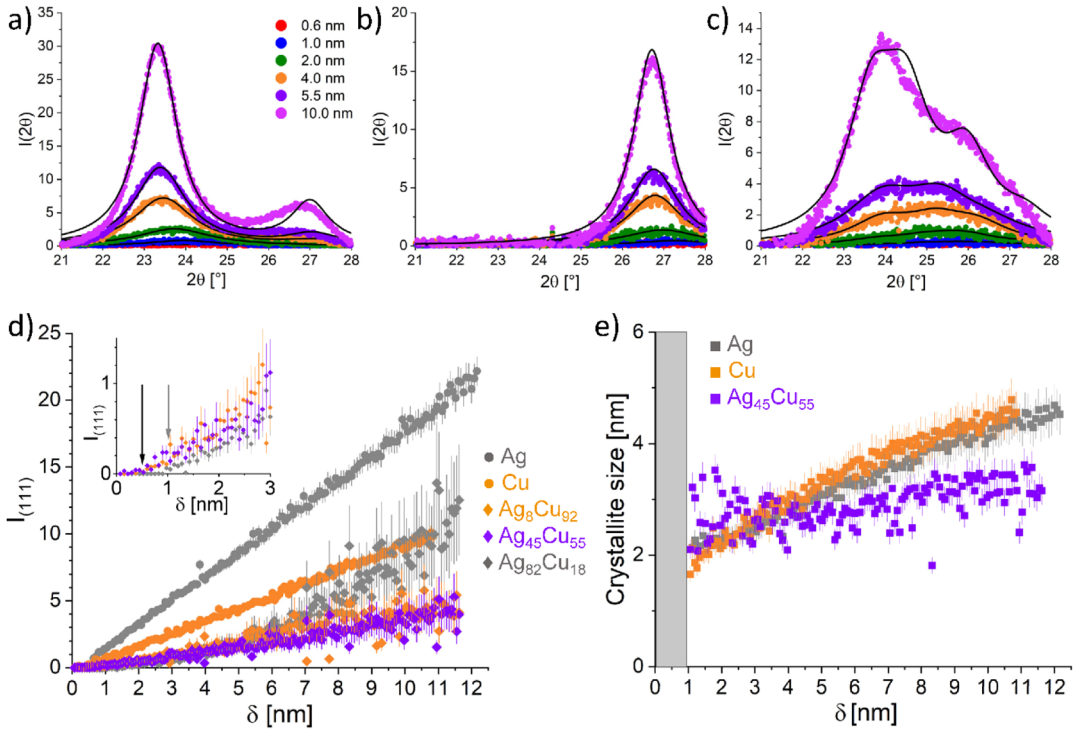

Figure 1. Cake cuts of the 2D GIWAXS data collected during sputter deposition of (a) Ag, (b) Cu, and (c) $Ag_{42}Cu_{58}$ for selected times indicated by the corresponding deposited thickness of 0.6, 1.0, 2.0, 4.0, 5.5, and 10.0 nm. The fits are cumulatively coupled fcc Bragg peaks considering the intensity and angular coupling between (111) and (200) peaks for reducing the degrees of freedom. (d) Extracted integrated intensity for the fitted (111) diffraction peak during deposition: ● Ag (gray), ● Cu (orange), ♦ Ag_8Cu_{92} (orange), ♦ $Ag_{45}Cu_{55}$ (violet), and ♦ $Ag_{82}Cu_{18}$ (gray). The inset shows the zoom-in of the integrated intensities found for the different (111) diffractions of the $Ag_{42}Cu_{58}$ specimen. The arrows denote the first onset of (111) intensity for Ag_xCu_{100-x} at around 0.5 nm (black: x = 8, x = 45) around 1 nm, (gray: x = 82). x denotes the Ag fraction in the alloy. (e) Extracted crystallite sizes using the Scherrer equation for Ag (gray), Cu (orange), and $Ag_{45}Cu_{55}$ (violet). The resolution for extracting the crystallite size is shown as a gray area.

covered by the detector (Figure 1b). In the case of $Ag_{42}Cu_{58}$, the GIWAXS pattern does not show well-separated peaks but a broad peak with shoulders (Figure 1c), which indicates that several crystalline phases are present during the deposition of the binary system. As deduced from the GIWAXS data of the metals, we may assume (111) face-centered cubic (fcc) Bragg peaks giving the main contribution. Following Vegard's law for calculating the lattice parameter in crystalline alloys[56]

$$d_{111}(Ag_xCu_{100-x}) = \frac{x}{100}d_{111}(Ag) + \left(1 - \frac{x}{100}\right)d_{111}(Cu) \quad (1)$$

expressing the composition of a mixture with x being Ag fraction in the alloy and a_{111} the respective pure metal bulk lattice parameters in (111) direction, one can calculate the $d_{111}(Ag_xCu_{100-x})$ lattice constant of the different crystalline phases present.[56] Based on this assumption, the final GIWAXS pattern has been modeled using three crystalline phases: Ag_xCu_{100-x} with x = 8 (Cu-rich phase) and $d_{111}(Ag_8Cu_{92})$ = 2.109 Å, 2θ = 26.142°; x = 45 (mixed phase with nearly nominal target composition) and $d_{111}(Ag_{45}Cu_{55})$ = 2.207 Å, 2θ = 25.03°; and x = 82 (Ag-rich phase) and $d_{111}(Ag_{82}Cu_{18})$ = 2.309 Å, 2θ = 23.838°. Please note that the compositions are deduced from the GIWAXS data, corresponding to the three diffraction peaks shown in Figure 1c. The different contributions to the GIWAXS signal for the alloy clusters are highlighted in Fig. S8 (Supporting Information). We estimate an uncertainty of ±3 (absolute) in phase composition, for example, $Ag_{45\pm3}Cu_{55\pm3}$. As seen in Figure 1d, the integrated intensities of the (111) peaks grow with the increase in deposited layer thickness, meaning that the deposited material is crystalline. Interestingly, the growth of the alloy particles clearly shows a phase separation in the above-mentioned three phases. The inset in Figure 1d depicts a delayed onset of the Ag-rich phase growth (indicated by the gray arrow), while the Cu-rich phase shows a traceable diffraction peak from around δ_{AgCu} = 0.5 nm on. In detail, upon the deposition of $Ag_{42}Cu_{58}$, in the early stages, we observe the growth of two types of crystallite fractions contributing to the diffraction signal. Both crystallites are considered as alloys. One type of crystallite has a composition of 92% Cu and 8% Ag. The second type of crystallite grows at the same time and has nearly the nominal composition with 45% Ag and 55% Cu. Thus, rather mixed alloy clusters with some Cu-rich crystalline core are initially established and grow in the early stages of $Ag_{42}Cu_{58}$ sputter deposition. From an effective thickness δ_{AgCu} = (1.0 ± 0.1) nm onward, growth of Ag-rich clusters set in (x = 82). The composition of 82% Ag and 18% Cu is as well consistent with an emerging Ag-dominated shell surrounding the Cu-rich phases in the core of the clusters. When a critical cluster size is reached, phase segregation occurs, and we obtain a Cu-rich core/Ag-rich shell internal structure of the clusters. These observations are consistent with MD simulations of AgCu alloy formation by Abraham and Bonitz.[46] The nominal composition solid solution structure is metastable.[48] The different compositions found in GIWAXS indicate a phase separation of the metastable nominal alloy composition clusters upon coalescence, when approaching the partial percolation thresh-

https://doi.org/10.1021/acsanm.1c04473
ACS Appl. Nano Mater. 2022, 5, 3832−3842

old. At the partial percolation threshold, one observes the beginning of partial coalescence of previously isolated clusters, which leads to ramification.[57] Due to the clusters' metastable state, upon touching each other, the phase segregation starts. This phase segregation is readily visible when the peak around 23.8° starts to emerge, indicating the onset of the formation of the Ag-rich phase. According to Chen and Zuo,[58] a Cu-rich phase and an Ag-rich phase exist in as-deposited films with a minimal thickness of 2.8 nm. Our results obtained during in situ sputter deposition show that the Ag-rich phase occurs after a deposition of 1 nm, which is close to the results by Chen and Zuo,[58] obtained by ex situ sputter deposition of $Ag_{50}Cu_{50}$ at a selected thickness investigated by TEM.

Figure 1e depicts estimates for lower limits of crystallite sizes of Ag, Cu, and $Ag_{45}Cu_{55}$ alloy deduced from the GIWAXS data based on the Scherrer analysis. Assuming changes in this size being representative for crystal sizes of Cu, Ag, and nearly nominal alloy composition domain phase, we note both, an increase in size for Ag and Cu, while the nominal alloy composition shows a significantly decreased growth. A cross-over point of the different cluster sizes is observed around a deposited thickness of 3 nm, when assuming that the clusters are mostly formed by crystalline material. This indicates a potential progressive phase separation during the alloy deposition, passing the partial percolation threshold. The crystallite size tends to be larger for Cu than for Ag. This might already indicate that the optical response as probed with surface differential reflectance spectroscopy (SDRS) will be dominated by Cu crystallites in the alloy layer, as Ag tends to be present as the major shell component.

The HRTEM image evaluation with respect to the composition of an $Ag_{42}Cu_{58}$ cluster is shown in Figure 2. Figure 2a displays an isolated $Ag_{42}Cu_{58}$ cluster with high circularity and a diameter of 5 nm at a deposited film thickness of 1 nm. The corresponding fast Fourier transformed (FFT) pattern (Figure 2b) reveals one dominating lattice plane distance of 0.229 nm, which can be designated to the {111}-planes. The FFT suggests a single solid solution with a spherical $Ag_{42}Cu_{58}$ cluster due to the lack of other spatial frequencies. In contrast, Figure 2c shows clusters, which have undergone coalescence at a deposited film thickness of 1 nm. From the corresponding FFT (Figure 2d), it turns out that two different phases are present in the coalesced particle. Again, the lattice fringes correspond to the {111}-planes. However, one set of {111}-planes relates to a lattice spacing of 0.200 nm, which belongs to a Cu-rich phase, whereas the other set with 0.234 nm belongs to an Ag-rich phase. Thus, the position of Cu- and Ag-rich domains are identified by means of inverse FFT (IFFT). The Ag-rich domain (Figure 2e) becomes visible by filtering out shorter frequencies (belonging to the Cu-rich phase) in the IFFT. To reveal the Cu-rich domains (Figure 2f), longer frequencies are filtered out. Importantly, the results presented in Figure 2 are representative for the majority of the investigated clusters. In the literature, it was reported that isolated clusters in the $Ag_{42}Cu_{58}$ film tended to exist in the form of a metastable solid solution;[41] clusters which were apparently forced to coalesce, tended to consist of separate phases. These earlier findings suggest that the phase separation of $Ag_{42}Cu_{58}$ clusters occurs when a certain critical volume is reached around the partial percolation threshold, where cluster coalescence prevails over surface diffusion of isolated clusters. Thus, the establishment of a boundary between two adjacent clusters fosters demixing via spinodal decomposition pathways

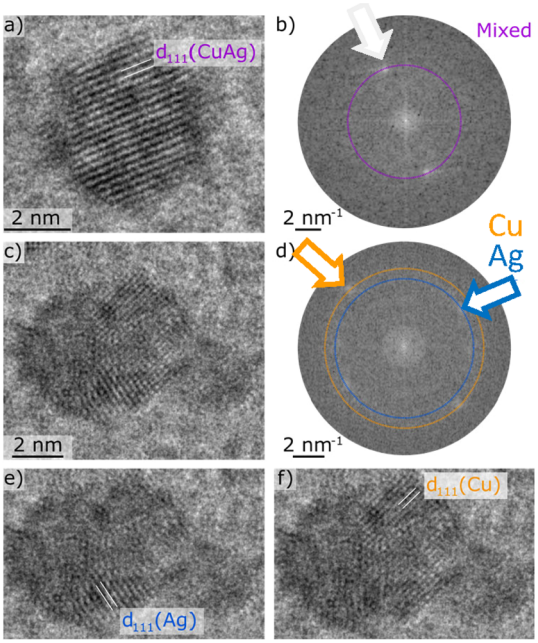

Figure 2. HRTEM images representing (a) an $Ag_{42\pm3}Cu_{58\pm3}$ cluster on a carbon layer on a TEM grid with high circularity and (c) an $Ag_{42}Cu_{58}$ cluster in the beginning state of coalescence. (b) FFT of the single cluster reveals the mixed state. The arrow hints at dominating frequencies (visible as maxima), which can be designated to the {111}-planes. The circle serves as a guide-to-the-eye for the iso-frequency positions in the FFT. (d) A demixed state is found for the coalesced clusters. The orange-outlined arrow points at the dominating frequency in the FFT of the Cu-rich phase, while the blue-outlined one corresponds to those of the Ag-rich phase. The frequencies are designated to the {111}-planes of the respective phases. The orange-/blue-dashed circles serve as guide-to-the-eye to visualize the iso-frequency positions in the FFT of the dominating frequencies. The circles are clearly separated. (e) IFFTs of image (d) disregarding frequencies, which correspond to the Cu-rich phase shows a Ag-rich regime in the coalesced cluster. (f) Second IFFT of image (d) shows the Cu-rich regime disregarding frequencies corresponding to the Ag-rich phase. (e) and (f) have the same scale as in (c). One set of {111}-planes relates to a lattice spacing of 0.200 nm, which belongs to a Cu-rich phase (d), whereas the other set with 0.234 nm belongs to an Ag-rich phase (d), while for CuAg, the lattice spacing is 0.229 nm, which can be designated to the {111}-planes (b).

over a wide composition range.[48] Hence, our investigations fully agree with the previous observations and, very importantly, they bridge the gap between MD simulated cluster growth and experiments with HRTEM.

In order to elucidate the growth kinetics, respectively, atomic mobilities and to obtain statistically averaged quantities, we complement the results from our GIWAXS and HRTEM measurements with in situ GISAXS measurements allowing for retrieving the local changes in cluster morphology during the sputter deposition. The GISAXS intensity distributions are proportional to lateral and parallel correlations in the electron density averaged over the macroscopically illuminated volume. Thus, the temporal evolution of the key scattering features (see Supporting Information Figures S1 and S2) decodes the growth kinetics and morphology averaged over approx. 10^{10} clusters at the same time. The nonequilibrium cluster growth morphology is modeled with geometrical assumptions of local monodisperse hemispherical clusters in a hexagonal arrange-

https://doi.org/10.1021/acsanm.1c04473
ACS Appl. Nano Mater. 2022, 5, 3832−3842

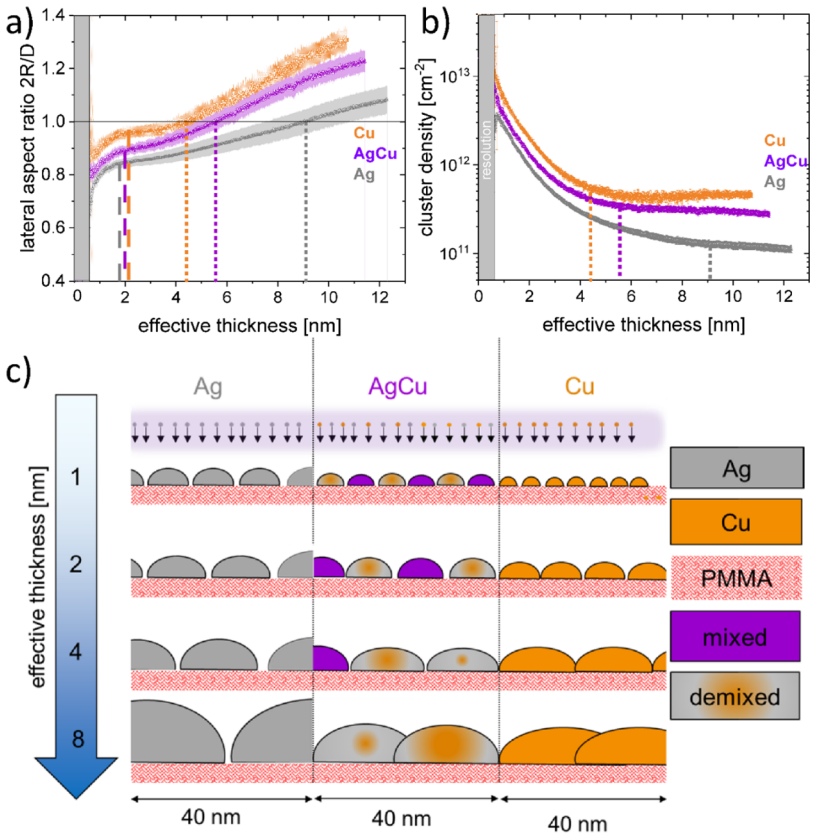

Figure 3. (a) Lateral aspect ratio of Ag (gray), Cu (orange), and nominal $Ag_{42}Cu_{58}$ (violet) clusters sputter-deposited on PMMA. Long-dashed lines indicate the partial percolation threshold and dotted lines indicate the percolation threshold. (b) Evolution of cluster density of Ag (gray), Cu (orange), and $Ag_{42}Cu_{58}$(violet). (c) Sketch for the local growth morphology of Ag, AgCu, and Cu on PMMA at 1, 2, 4, and 8 nm effective thicknesses.

ment acting as coherent scattering domains.[59] The model quantifies the evolution of interparticle distances D and cluster radii R as a function of the deposited effective layer thickness for each single and binary metal deposition (see Supporting Information, Figure S3). Due to the key scattering features in the 2D GISAXS pattern (see Figure S1b in Supporting Information), a hemispherical cluster shape is assumed. This is further justified by the extracted percolation thresholds for Cu and AgCu, which lie close to our previous results for Cu on a diblock copolymer film [polystyrene-*block*-poly(ethylene oxide), PS-*b*-PEO].[60] The hemispherical shape here compared to the vertically elongated Cu clusters found by Schaper et al.[60] on diblock-copolymer templates is attributed to the different metal−substrate interactions on PMMA homopolymer thin films compared to the diblock copolymer film in ref 52.

GISAXS allows for observing average electron densities. Figure 3a shows the thickness-dependent evolution of the ratio cluster diameter ($2R$) to an interparticle distance (D) of the Ag, Cu, and AgCu clusters during the sputter deposition as probed by GISAXS. The position of the first local maxima around 2 nm yields the partial percolation threshold,[61] indicated by the dashed lines. The onset of the full percolation is given by the critical thickness, where $2R/D = 1$ is indicated by solid lines. The latter one denotes the insulator-to-metal transition by providing a macroscopic electrically conductive pathway.[62] As expected for a composition of 42:58 (Ag−Cu) of the deposited materials, the percolation threshold of $Ag_{42}Cu_{58}$ lies between that of Cu and Ag with Cu percolating at a lower thickness. This corroborates our recent findings.[60,62]

All three curves show a typical four-stage growth behavior.[63] Below 2 nm, we observe a diffusion-mediated growth, which is indicated by an increase of $2R/D$. This growth levels off in maxima, which indicate the transition to the adsorption-mediated regime. Here, isolated clusters reach a critical size, where the merging of two clusters takes longer time. This growth mode leads to dumb-bell-shaped elongated clusters. The growth via adsorption continues until the percolation threshold, where a network of interconnected clusters is established. While the partial percolation threshold allows for retrieving values of the cluster mobility, the percolation threshold yields information on the coalescence velocity. The lower atomic mobility of Cu compared to Ag can be regarded as Cu being more cohesive and leads to the observed earlier percolation threshold. We note that the deposition rates of Ag, Cu, and AgCu are slightly different (within 0.01 nm/s) due to the used electronics of the sputter chamber, but these differences do not influence the percolation threshold as discussed in earlier work.[53] Hence, the observed shift of the percolation threshold uniquely depends on the material compositions (Ag, Cu, and AgCu). The critical cluster radii and partial percolation thresholds following Jeffers et al.[57] are for Cu $\delta_{c,Cu} = 2.1$ nm, $R_c = 3.7$ nm, for $Ag_{42}Cu_{58}$ $\delta_{c,Ag_{42}Cu_{58}} = 2.0$ nm, $R_c = 4.1$ nm, and for Ag $\delta_{c,Ag} = 1.8$ nm, $R_c = 4.2$ nm. The consequence is as follows. Cu clusters are less mobile and have a lower surface diffusion coefficient.[64] Hence, they show a larger cluster density at early stages (see Table S3 in the Supporting Information). In addition, the Cu clusters need more time to fully coalesce. Hence, the Cu clusters spread over

https://doi.org/10.1021/acsanm.1c04473
ACS Appl. Nano Mater. 2022, 5, 3832−3842

a larger scale and the percolation threshold is reduced compared to pure Ag deposition. Ag shows the higher (relative) mobility and faster coalescence kinetics, leading to shift of the percolation threshold to higher values and a lower cluster density. $Ag_{42}Cu_{58}$ clusters shows intermediate kinetics and percolation threshold. In ref 48, clusters below $R < 2.5$ nm grow as solid metastable solutions. Upon the onset of coalescence of clusters, phase segregation occurs. The demixing is induced by the coalescence of critical-sized clusters with diameters around 7.4−8.4 nm, that is, the diameter ($2R_c$) of the clusters at the partial percolation threshold. This corresponds well to recent results on phase-separating nanoalloys,[65] predicting a critical particle diameter of 8 nm at equal composition of the components. We determine experimentally 8.2 nm, which is in excellent agreement.

Concerning the cluster mobility, the reference value up to now is (for gold): $D_S = 7.33 \times 10^{-18}$ m^2/s.[61] In this earlier work on sputter deposition of gold, the partial percolation threshold was 1.9 nm.[61] We follow Jeffers et al.[57] using the liquid surface tension for estimating the diffusion coefficient. Using the relation $\delta \approx J \times t_c$ relating deposited thickness δ, deposition rate J, and critical time t_c (the time of the partial percolation threshold), we estimate the effective diffusion coefficient or effective mobility via

$$D_S \approx \frac{k_B T J R_c^4}{\alpha \delta_c \gamma \Omega^{4/3}} \quad (2)$$

This value is the average of many cluster sizes and estimated at room temperature. δ_c and R_c are determined by GISAXS data. γ is deduced from tabulated values and weighted according to the composition (see Table S3 in the Supporting Information). We note that we used $k_BT = 4.1 \times 10^{-21}$ J, corresponding to $T = 296$ K, which corresponds to the substrate temperature following Jeffers et al.[57] In case of thermal deposition under equilibrium conditions, a factor of 100:1 in atomic mobility of Ag to Cu is observed.[64] This is not the case in the present study, confirming the nonequilibrium conditions during sputter deposition. We note, that the Jeffers model makes use of the metal-on-metal surface diffusion. The local maximum in $2R/D$, see Figure 3a around a deposited thickness of $\delta = 2$ nm, allows for an experimental determination of the elongation transition (ramification).[49,50] At the same time, the partial percolation threshold depends on the metal−polymer interaction. This give rise to a different critical radius R_c when depositing the different materials.

The results are as follows (see also Table 3 in the Supporting Information) for the diffusion coefficient: $D_{S,Ag} = 2.57 \times 10^{-18}$ m^2/s, $D_{S,Ag_{42}Cu_{58}} = 2.61 \times 10^{-18}$ m^2/s, and $D_{S,Cu} = 1.97 \times 10^{-18}$ m^2/s. These values show that Cu is ∼25% less mobile with Ag being more mobile. Thus, the mobility of the atoms on the cluster surface of the metastable alloy clusters is dominated by Ag atoms preferentially located at the cluster boundaries. Cu atoms located in the core are much less mobile. In addition, the internal decomposition potential may already act in the early stages as a driving force for the enhancement of atomic displacements on a substrate material. One should note, however, that the used model represents a semiquantitative calculation and yields a lower boundary for the determined mobilities. The model does not consider the pinning of the clusters on the substrate or grain boundary effects nor substrate heterogeneities. Yet, using the same substrate and different target compositions, we can at least deduce and compare relative mobilities during the sputter deposition process. Concerning the influence of surface energies, a rule of thumb yields that materials having a higher surface energy are coated by materials with lower surface energy in bimetallic cluster systems.[66] Table S3 confirms this rule, as Ag (0.95 J/m^2) coats Cu (1.35 J/m^2), leading to the core−shell structure regardless of the initial size of the clusters;[67] MD and other simulations show that differences in surface energies drive the formation of Ag shell Cu core morphologies. Indeed, our in situ measurements show that mixed clusters are present in the beginning, which evolve into a core shell morphology for radii > 6 nm, which corroborates the findings in ref 67. This confirms that controlled cluster coalescence allows for fabrication alloy clusters of with unique, patterned core/shell morphology being a vital ingredient for anticounterfeiting.

Sputter deposition is an out-of-equilibrium process. An equilibrium state necessary for phase diagram predictions will not be reached. The substrate temperature is at room temperature but the kinetic energy of the sputtered atoms would yield a temperature of ∼1000 K.[54] Thermalization and interactions on the nanoscale with the substrate as well as surface and boundary effects[41] come into play. Hence, the phase diagram (being established for bulk) gives a hint for the tendency of demixing, but the absolute value of percentage will be much different.

The cluster density during deposition is shown in Figure 3b. For $\delta_{Ag_{42}Cu_{58}} < 1$ nm, the $Ag_{42}Cu_{58}$ cluster density follows closely the Cu cluster density trend. For 1 nm < $\delta_{Ag_{42}Cu_{58}} < 2.5$ nm, the cluster density of $Ag_{42}Cu_{58}$ follows the trend of the Ag cluster density. For $\delta_{AgCu} > 2.5$ nm beyond the partial percolation threshold, the $Ag_{42}Cu_{58}$ cluster density seems to be dominated by Cu. This finding is consistent with the reports that surface atomic mobility for Ag is approximately a factor 100 larger than for Cu, leading to lower cluster density.[64] It also matches well with the mobilities discussed above. Close to the nucleation threshold, we observe the following cluster densities at a deposited thickness of 0.75 nm (see Table S3, Supporting Information): $\rho/[cm^{-2}] = 3.5 \times 10^{12}$ (Ag)/9.2×10^{12} (Cu)/5.9×10^{12} ($Ag_{42}Cu_{58}$) (Figure 3b). The cluster density increases by a factor of 2.6. Taking a molar fraction of Ag−Cu of 42:58, $\rho_{Ag_{42}Cu_{58}}$ would yield 6.8×10^{12} cm^{-2}, being in very good agreement with the measured data. Concerning the percolation threshold, a similar calculation would yield 6.4 nm instead of 5.5 nm. This proves that the slowest component (Cu) primarily influences the growth kinetics until the percolation threshold.

Both partial and percolation thresholds of $Ag_{42}Cu_{58}$ tend to be more similar to Ag. This finding suggests a simplified vision of alloy cluster growth: first, copper clusters are established. Then, adsorbed silver being more mobile attaches to the emerging copper nuclei or core clusters. This leads first to a mixture with a trend of Ag being more likely present on the surface of the clusters and at the interface to the substrate material. Such a Cu-core and Ag-shell cluster morphology is corroborated by MD simulations obtained by Abraham et al.[46] In our experiment presented here, we observe these mechanisms in real-time. To summarize, Cu being the less mobile species will be responsible for the structure formation, leading to the domination of Cu regarding the percolation threshold.

Figure 3c depicts the model of cluster growth during alloy sputter deposition. The nonequilibrium shape of the clusters is

https://doi.org/10.1021/acsanm.1c04473
ACS Appl. Nano Mater. 2022, 5, 3832−3842

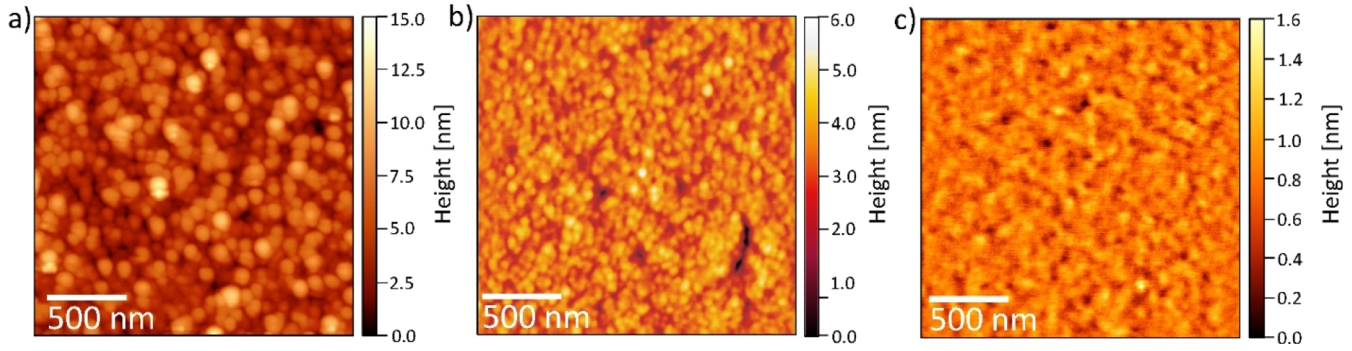

Figure 4. AFM topography of (a) Ag on PMMA, (b) Cu on PMMA, and (c) $Ag_{42}Cu_{58}$ alloy sputter-deposited on PMMA (δ_{Ag} = 12.3 nm, δ_{Cu} = 10.7 nm, $\delta_{Ag_{42}Cu_{58}}$ = 11.4 nm).

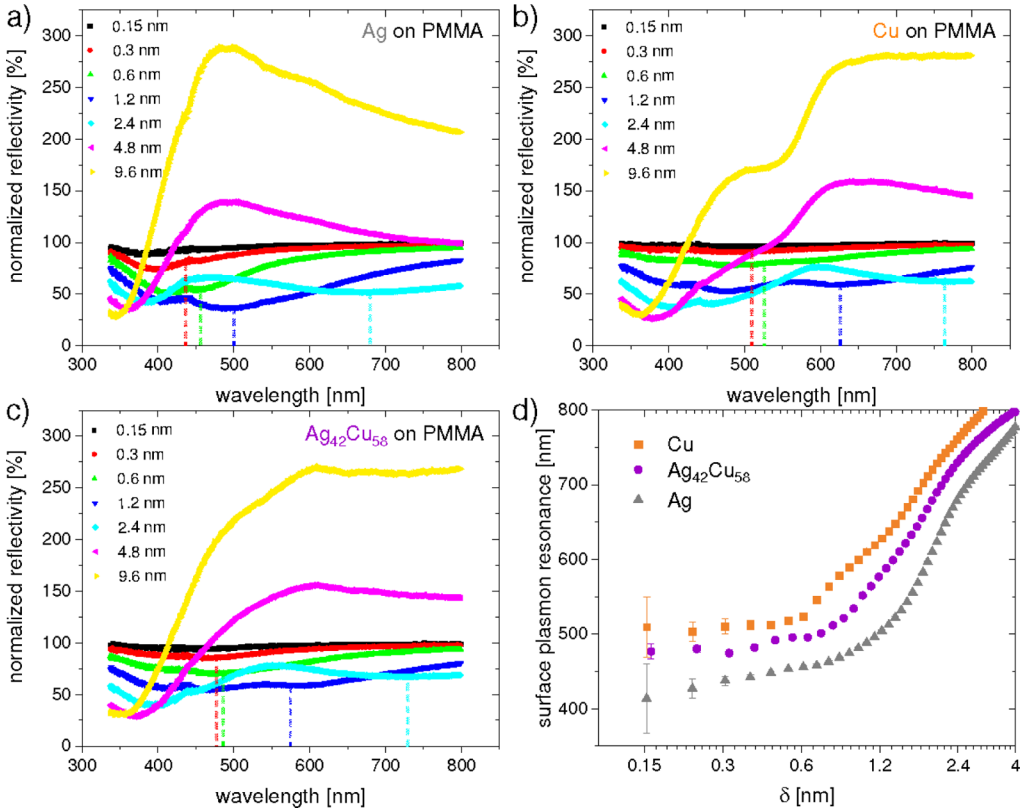

Figure 5. Surface-differential UV−vis reflectance spectra for (a) Ag, (b) Cu, and (c) $Ag_{42}Cu_{58}$ sputter-deposited on 80 nm PMMA/SiO_2/Si templates with selected effective metal layer thicknesses as indicated. The wavelength of a predominant SPR is indicated with a dashed line. (d) Evolution of the predominant SPR as a function of deposited film thickness.

hemispherical during the sputter deposition. Below the partial percolation threshold around 2 nm, alloy clusters are growing with nearly nominal and a copper-rich composition. This growth type is indicated by the violet color (nominal composition) and the gray (Ag) and orange (Cu) colors, respectively. Upon the partial percolation threshold around 2 nm, the metastable mixed clusters start to coalesce and a phase separation induced by spinodal decomposition into Ag-rich and Cu-rich domains occurs.[48,58] This process is indicated for a thickness of 4 nm. Nominal composition clusters are still present; but at 8 nm, well beyond the partial percolation threshold, predominantly silver-rich and copper-rich clusters exist. Additionally, the lateral aspect ratios between diameter and distance including percolation behavior are presented: pure Cu percolates first, then percolates the alloy, and finally Ag above 8 nm.

AFM topography images are presented in Figure 4a−c. The results show the different nanogranular structures for the final thicknesses and corroborate the cluster size findings from GISAXS. In detail, we observe larger silver clusters > 30 nm with a larger distance (Figure 4a) and smaller Cu clusters in a smaller distance (Figure 4b). Accordingly, $Ag_{42}Cu_{58}$ shows intermediate distances and sizes, yet more similar to Cu (Figure 4c). Accordingly, the sputter-deposited Ag film shows a much larger roughness (see Table S2, Supporting Information) compared to Cu and $Ag_{42}Cu_{58}$ films. This observation corroborates that the structure formation during alloy sputter-deposition is dominated by Cu cores. For deposited thicknesses of δ_{AgCu} = 0.5 and 1 nm (Figure S4,

https://doi.org/10.1021/acsanm.1c04473
ACS Appl. Nano Mater. 2022, 5, 3832−3842

Supporting Information), the extracted sizes of clusters using TEM are (2.7 ± 0.5) and (4.5 ± 0.5) nm, respectively. These values fit well with the minimum crystallite size for $Ag_{42}Cu_{58}$ found to be (3.0 ± 1.0) nm (Figure 1e) and a cluster size derived from GISAXS (Figure S3), $2R$ = (4.0 ± 0.1) nm.

To enable an application of the sputter deposited films, the morphological and compositional parameters of the metal clusters are correlated with the optoelectronic properties of the clusters, namely, the plasmon resonance. The correlation is obtained by simultaneously (together with GISAXS and GIWAXS) measuring in situ specular UV−vis reflectance data normalized to the pristine optical reflectivity. These so-called SDRS data are presented in Figure 5, while Figure S2 (Supporting Information) yields an overview in terms of color-coded contour maps of the combined in situ GISAXS, GIWAXS, and SDRS measurements during sputter deposition. For a more detailed analysis, Figures 5a,b depicts the SDRS spectra for Ag and Cu on PMMA as a function of selected deposited thickness. Simulated spectra for growing layers of Ag, Cu, and AgCu on PMMA (80 nm)/SiO_2 (2 nm)/Si layers based on complex matrix formalism using Fresnel equations (reflectance calculator, Filmetrics, filmetrics.com) are presented in Figure S5 (Supporting Information). It is deduced that the minima below 400 nm and their blue shift is dominated by optical thin-film interference (TFI) for the pure metal layers.[16] The minima close to the resonance position marked with a star in Figure 5a,b cannot be simulated in the framework of simple matrix formalism as an effective medium and thus is associated with the plasmon resonance. Hence, we focus on observing absorption features above 420 nm to trace plasmonic activity during growth. We fit the obtained spectra (Figure S6, Supporting Information) and extract the surface plasmon resonance (SPR) position for Ag, Cu, and $Ag_{42}Cu_{58}$ as a function of deposited film thickness (Figure 5d). In all cases, we observe at the onset of metal deposition a broad decrease of reflectivity with a local minimum above 420 nm, which red shifts only slightly at effective thicknesses below 0.6 nm. The same holds for $Ag_{42}Cu_{58}$ in Figure 5c. The red shift of the minimum is associated with the Mie shift of a SPR induced by the nanoscale size of the metallic clusters.[68−71] After 0.6 nm effective thickness, the SPR shift increases significantly until a deposited thickness of around 2 nm, which complies with the partial percolation threshold as extracted from GISAXS outlined above. Afterward, the slope of the SPR position as a function of deposited metal thickness is gradually reduced. This common trend might be correlated to grain boundaries acting as defects and the partial coalescence of the clusters reshaping the isolated clusters to laterally elongated clusters. Although the course of the observed SPR shifts are relatively similar, the SPR frequency starts at different positions depending on the material-specific electrical permittivity of the cluster's effective medium. The SDRS spectra and the SPR position for the alloy seems to be more dominated by the Cu fraction, respectively, the Cu-cores. Clearly, the plasmon resonance of $Ag_{42}Cu_{58}$ is located approximately 30 nm below the SPR of Cu and approximately 40 nm above Ag for all thicknesses. This observation is consistent with an effective 4/7 Cu, respectively, 3/7 Ag mol fraction of the clusters and complies with the findings of Beyene et al.,[41] where the Cu content of the clusters tunes the extinction. Note that, the strongest decrease in normalized reflectivity occurs for all three depositions around an effective thickness of 2 nm signifying best surface-enhanced Raman scattering performance at the partial percolation threshold. However, the plasmonic properties of alloy nanoparticles are less pronounced compared to pure Ag nanogranular thin films because of the damping of the plasmon resonance in alloyed clusters due to the scattering of the valence electrons at the internal boundaries. Thus, a fine-tuning of the plasmon resonance is possible not only by the shape of the metal clusters but also by the composition using alloying. In order to avoid effects of friction and storage, transparent protective coatings[55,72] are needed for long-term stability in the final application. This avoids structural modification of island films. For CuAg clusters, we observe a 10% shift and a damping of the plasmon resonance for CuAg alloy clusters. A short discussion is presented in the Supporting Information. Hence, such alloy clusters are very interesting for anticounterfeiting applications because only very advanced analysis tools will allow to detect the alloy composition, whereas the sputter deposition using alloy targets in combination with the detailed knowledge about the growth laws enables a very precise and large-scale deposition of the alloy clusters.

CONCLUSIONS

We present a real-time in situ study of the phase-separation of AgCu alloy clusters during sputter deposition on PMMA. Using a combination of ex situ TEM, in situ optical spectroscopy, and combined time-resolved GISAXS/GIWAXS, we are able to directly observe and quantify the onset of different phases and their composition occurring due to the spinodal decomposition of the alloy. Around the partial percolation threshold, the majority of AgCu clusters undergo phase-separation induced by the predominance of incomplete coalescence phenomena. A Cu-rich core and Ag-rich shell morphology is established for the alloy clusters. For the first time, we are able to deduce effective diffusion coefficients, which clearly corroborate theoretical assumptions on the phase separation process. To enhance the material contrast between metals in the alloy, future studies using anomalous GISAXS might be an option.[73] Yet, we are able to deduce the changing composition of the different phases as a function of deposited thickness and the delayed onset of the growth of the Ag-rich phase. The core−shell morphology clearly affects the mobility of the alloy clusters, being dominated by the Ag atoms. We uniquely correlate our morphological and compositional findings with the tunability of the plasmon resonance of the different materials, including the alloy. The tunability of the plasmon resonances by cluster composition, a crucial prerequisite for anticounterfeiting, has been shown in a previous work.[41] According to Walter et al.,[55] such plasmon resonance-based structural color can be applied in anti-counterfeiting. Spectral response is determined by the plasmon resonances' spectral shape and position and the variation of the spacer layer on top of a mirroring substrate. This approach is combined here with the combination of color and a unique alloy nanostructure as an additional security feature. Importantly, our setup consisting of metal alloy clusters/PMMA spacer layer/silicon as mirror substrate is a multilayer system, which is compatible with roll-to-roll technology for mass production.[72] Our quantitative findings in terms of cluster mobility yield the necessary input for MD simulations used for predictive material science. With Cu being the structure-defining component and Ag predominantly in the shell, our findings offer the potential to partially decouple structural (distance) effects on the one hand and size- and

https://doi.org/10.1021/acsanm.1c04473
ACS Appl. Nano Mater. 2022, 5, 3832−3842

composition-related influences on the plasmon resonance in directly deposited, high density, organic shell-free cluster layers used in organic photovoltaics and electronics.

■ ASSOCIATED CONTENT

Supporting Information

The Supporting Information is available free of charge at https://pubs.acs.org/doi/10.1021/acsanm.1c04473.

Sputter deposition parameters; roughness determined by AFM; details of the GISAXS/GIWAXS experiments; overview of GISAXS, GIWAXS, and SDRS data; histograms of particle sizes from TEM; details of the analysis of SDRS; radius and distance of the GISAXS analysis; GIWAXS data analysis; and parameters used for Jeffers' kinetic freezing model (PDF)

■ AUTHOR INFORMATION

Corresponding Author

Stephan V. Roth − *Deutsches Elektronen-Synchrotron DESY, D-22607 Hamburg, Germany; Department of Fibre and Polymer Technology, KTH Royal Institute of Technology, 10044 Stockholm, Sweden;* orcid.org/0000-0002-6940-6012; Phone: +4940/8998-2934; Email: stephan.roth@desy.de, svroth@kth.se

Authors

Matthias Schwartzkopf − *Deutsches Elektronen-Synchrotron DESY, D-22607 Hamburg, Germany;* orcid.org/0000-0002-2115-9286

André Rothkirch − *Deutsches Elektronen-Synchrotron DESY, D-22607 Hamburg, Germany*

Niko Carstens − *Lehrstuhl für Materialverbunde, Institut für Materialwissenschaft, Christian-Albrechts-Universität zu Kiel, D-24143 Kiel, Germany*

Qing Chen − *Deutsches Elektronen-Synchrotron DESY, D-22607 Hamburg, Germany; School of Chemistry and Material Science, University of Science and Technology of China, 230026 Hefei, China*

Thomas Strunskus − *Lehrstuhl für Materialverbunde, Institut für Materialwissenschaft, Christian-Albrechts-Universität zu Kiel, D-24143 Kiel, Germany;* orcid.org/0000-0003-3931-5635

Franziska C. Löhrer − *Lehrstuhl für Funktionelle Materialien, Physik-Department, Technische Universität München, D-85748 Garching, Germany*

Senlin Xia − *Lehrstuhl für Funktionelle Materialien, Physik-Department, Technische Universität München, D-85748 Garching, Germany;* orcid.org/0000-0002-6259-0689

Christoph Rosemann − *Deutsches Elektronen-Synchrotron DESY, D-22607 Hamburg, Germany*

Lorenz Bießmann − *Lehrstuhl für Funktionelle Materialien, Physik-Department, Technische Universität München, D-85748 Garching, Germany;* orcid.org/0000-0002-1046-1236

Volker Körstgens − *Lehrstuhl für Funktionelle Materialien, Physik-Department, Technische Universität München, D-85748 Garching, Germany;* orcid.org/0000-0001-7178-5130

Shiwani Ahuja − *Deutsches Elektronen-Synchrotron DESY, D-22607 Hamburg, Germany*

Pallavi Pandit − *Deutsches Elektronen-Synchrotron DESY, D-22607 Hamburg, Germany*

Jan Rubeck − *Deutsches Elektronen-Synchrotron DESY, D-22607 Hamburg, Germany*

Susann Frenzke − *Deutsches Elektronen-Synchrotron DESY, D-22607 Hamburg, Germany*

Alexander Hinz − *Lehrstuhl für Materialverbunde, Institut für Materialwissenschaft, Christian-Albrechts-Universität zu Kiel, D-24143 Kiel, Germany*

Oleksandr Polonskyi − *Lehrstuhl für Materialverbunde, Institut für Materialwissenschaft, Christian-Albrechts-Universität zu Kiel, D-24143 Kiel, Germany;* Present Address: Oleksandr Polonskyi, 3324 Engineering 2, University of California Santa Barbara, Santa Barbara, CA 93106-5080, United States

Peter Müller-Buschbaum − *Lehrstuhl für Funktionelle Materialien, Physik-Department, Technische Universität München, D-85748 Garching, Germany; Heinz Maier-Leibnitz Zentrum (MLZ), Technische Universität München, D-85748 Garching, Germany;* orcid.org/0000-0002-9566-6088

Franz Faupel − *Lehrstuhl für Materialverbunde, Institut für Materialwissenschaft, Christian-Albrechts-Universität zu Kiel, D-24143 Kiel, Germany;* orcid.org/0000-0003-3367-1655

Complete contact information is available at: https://pubs.acs.org/10.1021/acsanm.1c04473

Author Contributions

M.S. T.S., F.L., S.X., V.K., P.P., S.F., J.R., A.H., and O.P. conducted the experimental campaigns at P03, PETRA III. N.C., A.H., and L.B. performed electron microscopy measurements. Q.C. performed the AFM measurements and N.C. and A.H. the TEM measurements. M.S. performed the UV−vis analysis. A.R., M.S., C.R., and S.V.R. conducted the GIWAXS analysis. M.S., S.A., P.P., and S.V.R. conducted the GISAXS analysis. S.V.R., P.M.B., and F.F. planned and devised the experiments. The manuscript was written with contributions from all authors.

Funding

The authors acknowledge the Deutsche Forschungsgemeinschaft (DFG) for funding under the projects RO 4638/1-2, FA 234/23-2, and MU 1487/18-2.

Notes

The authors declare no competing financial interest.

■ ACKNOWLEDGMENTS

We thank Björn Fricke (DESY) for help during the experiments. We thank Lorenz Kienle (CAU Kiel) for help in the TEM measurements. Parts of this research were carried out at the light source PETRA III at DESY, a member of the Helmholtz Association (HGF). We thank Manuel Reus (TUM) for help with the GIWAXS analysis.

■ REFERENCES

(1) Amarandei, G.; O'Dwyer, C.; Arshak, A.; Thiele, U.; Steiner, U.; Corcoran, D. Effect of Au Nanoparticle Spatial Distribution on the Stability of Thin Polymer Films. *Langmuir* **2013**, *29*, 6706−6714.

(2) Khitous, A.; Lin, C.-F.; Kameche, F.; Zan, H.-W.; Malval, J.-P.; Berling, D.; Soppera, O. Plasmonic Au Nanoparticle Arrays for Monitoring Photopolymerization at the Nanoscale. *ACS Appl. Nano Mater.* **2021**, *4*, 8770−8780.

(3) Kuzminova, A.; Solař, P.; Kúš, P.; Kylián, O. Double Plasmon Resonance Nanostructured Silver Coatings with Tunable Properties. *J. Nanomater.* **2019**, *2019*, 1−8.

(4) Bauer, G.; Hassmann, J.; Walter, H.; Haglmüller, J.; Mayer, C.; Schalkhammer, T. Resonant Nanocluster Technology—from Optical Coding and High Quality Security Features to Biochips. *Nanotechnology* **2003**, *14*, 1289−1311.
(5) Camelio, S.; Babonneau, D.; Vandenhecke, E.; Louarn, G.; Humbert, B. Linear Chains of Ag Nanoparticles Embedded in Dielectric Films for SERS Applications in Analytical Chemistry. *Nanoscale Adv.* **2021**, *3*, 6719−6727.
(6) Spalatu, N.; Hiie, J.; Maticiuc, N.; Krunks, M.; Katerski, A.; Mikli, V.; Sildos, I. Plasmonic Effect of Spray-Deposited Au Nanoparticles on the Performance of CSS CdS/CdTe Solar Cells. *Appl. Surf. Sci.* **2015**, *350*, 69−73.
(7) Pan, S.; Yang, Z.; Chen, P.; Deng, J.; Li, H.; Peng, H. Wearable Solar Cells by Stacking Textile Electrodes. *Angew. Chem., Int. Ed.* **2014**, *53*, 6110−6114.
(8) Vahl, A.; Strobel, J.; Reichstein, W.; Polonskyi, O.; Strunskus, T.; Kienle, L.; Faupel, F. Single Target Sputter Deposition of Alloy Nanoparticles with Adjustable Composition via a Gas Aggregation Cluster Source. *Nanotechnology* **2017**, *28*, 175703.
(9) Rocha-Rocha, O.; Cortez-Valadez, M.; Calderón-Ayala, G.; Martínez-Nuñez, C. E.; Pedroza-Montero, M.; Flores-Acosta, M. Confined Clustering of AuCu Nanoparticles under Ambient Conditions. *Phys. Lett. A: Gen. At. Solid State Phys.* **2019**, *383*, 125985.
(10) Lee, S.; Lee, W.; Jung, H.-T.; Ross, C. A. Selective Deposition of Copper on Self-Assembled Block Copolymer Surfaces via Physical Vapor Deposition. *ACS Appl. Mater. Interfaces* **2021**, *13*, 52931−52937.
(11) Kim, S. H.; Rho, Y.; Cho, E.; Myung, J. S.; Lee, S.-J. Surface Plasmonic Resonance Tunable Nanocomposite Thin Films Applicable to Color Filters, Heat Mirrors, Semi-Transparent Electrodes, and Electromagnetic-Shields. *Nanoscale* **2021**, *13*, 12260−12270.
(12) Li, D.; Han, W.; Yuan, Y.; Zhao, Y.; Cheng, Z.; Chen, J. Tunable Optical Response Based on Au@GST Core-Shell Hetero-Nanostructures. *ACS Appl. Nano Mater.* **2021**, *4*, 9123−9131.
(13) Smith, A. F.; Skrabalak, S. E. Metal Nanomaterials for Optical Anti-Counterfeit Labels. *J. Mater. Chem. C* **2017**, *5*, 3207−3215.
(14) Kharkwal, A.; Deepa, M.; Joshi, A. G.; Srivastava, A. K. Red to Blue High Electrochromic Contrast and Rapid Switching Poly(3,4-Ethylenedioxypyrrole)-Au/Ag Nanocomposite Devices for Smart Windows. *ChemPhysChem* **2011**, *12*, 1176−1188.
(15) Abraham, J. W.; Strunskus, T.; Faupel, F.; Bonitz, M. Molecular Dynamics Simulation of Gold Cluster Growth during Sputter Deposition. *J. Appl. Phys.* **2016**, *119*, 185301.
(16) Schwartzkopf, M.; Wöhnert, S.-J.; Waclawek, V.; Carstens, N.; Rothkirch, A.; Rubeck, J.; Gensch, M.; Drewes, J.; Polonskyi, O.; Strunskus, T.; Hinz, A. M.; Schaper, S. J.; Körstgens, V.; Müller-Buschbaum, P.; Faupel, F.; Roth, S. V. Real-Time Insight into Nanostructure Evolution during the Rapid Formation of Ultra-Thin Gold Layers on Polymers. *Nanoscale Horiz.* **2021**, *6*, 132−138.
(17) Schuster, C.; Rennhofer, H.; Amenitsch, H.; Lichtenegger, H. C.; Jungbauer, A.; Tscheliessing, R. Metal−Insulator Transition of Ultrathin Sputtered Metals on Phenolic Resin Thin Films: Growth Morphology and Relations to Surface Free Energy and Reactivity. *Nanomaterials* **2021**, *11*, 589.
(18) Goetz, S.; Bauch, M.; Dimopoulos, T.; Trassl, S. Ultrathin Sputter-Deposited Plasmonic Silver Nanostructures. *Nanoscale Adv.* **2020**, *2*, 869−877.
(19) Yu, Q.; Zhang, J.; Wang, T.; Park, M.; Dong, H.; Chen, S.; Zhang, X.; Guo, S.; Li, Y. Y.; Zeng, Q.; Yang, Y. Transformation of Freestanding Carbon-Containing Gold Nanosheets into Au Nanoparticles Encapsulated within Amorphous Carbon: Implications for Surface Modification of Complex-Shaped Materials and Structures. *ACS Appl. Nano Mater.* **2021**, *4*, 5098−5105.
(20) Erb, D. J.; Schlage, K.; Röhlsberger, R. Uniform Metal Nanostructures with Long-Range Order via Three-Step Hierarchical Self-Assembly. *Sci. Adv.* **2015**, *1*, No. e1500751.
(21) Schmitt, P.; Stempfhuber, S.; Felde, N.; Szeghalmi, A. V.; Kaiser, N.; Tünnermann, A.; Schwinde, S. Influence of Seed Layers on the Reflectance of Sputtered Aluminum Thin Films. *Opt. Express* **2021**, *29*, 19472.
(22) Ramachandran, R. K.; Dendooven, J.; Detavernier, C. Controlled Synthesis of Fe-Pt Nanoalloys Using Atomic Layer Deposition. *Nanotechnology* **2021**, *32*, 095602.
(23) Gao, S.; Hao, S.; Huang, Z.; Yuan, Y.; Han, S.; Lei, L.; Zhang, X.; Shahbazian-Yassar, R.; Lu, J. Synthesis of High-Entropy Alloy Nanoparticles on Supports by the Fast Moving Bed Pyrolysis. *Nat. Commun.* **2020**, *11*, 2016.
(24) Lukehart, C. M.; Milne, S. B.; Stock, S. R.; Shull, R. D.; Wittig, J. E. Nanocomposites Containing Nanoclusters of Fe2P or γ-Fe2O3. *Mater. Sci. Eng., A* **1995**, *204*, 176−180.
(25) Li, G.; Luo, Y. Preparation and Characterization of Dendrimer-Templated Ag-Cu Bimetallic Nanoclusters. *Inorg. Chem.* **2008**, *47*, 360−364.
(26) Martínez, L.; Lauwaet, K.; Santoro, G.; Sobrado, J. M.; Peláez, R. J.; Herrero, V. J.; Tanarro, I.; Ellis, G. J.; Cernicharo, J.; Joblin, C.; Huttel, Y.; Martín-Gago, J. A. Precisely Controlled Fabrication, Manipulation and in-Situ Analysis of Cu Based Nanoparticles. *Sci. Rep.* **2018**, *8*, 7250.
(27) Solař, P.; Polonskyi, O.; Olbricht, A.; Hinz, A.; Shelemin, A.; Kylián, O.; Choukourov, A.; Faupel, F.; Biederman, H. Single-Step Generation of Metal-Plasma Polymer Multicore@shell Nanoparticles from the Gas Phase. *Sci. Rep.* **2017**, *7*, 8514.
(28) Liu, Y.; Padmanabhan, J.; Cheung, B.; Liu, J.; Chen, Z.; Scanley, B. E.; Wesolowski, D.; Pressley, M.; Broadbridge, C. C.; Altman, S.; Schwarz, U. D.; Kyriakides, T. R.; Schroers, J. Combinatorial Development of Antibacterial Zr-Cu-Al-Ag Thin Film Metallic Glasses. *Sci. Rep.* **2016**, *6*, 26950.
(29) Padovani, S.; D'Acapito, F.; Cattaruzza, E.; De Lorenzi, A.; Gonella, F.; Mattei, G.; Maurizio, C.; Mazzoldi, P.; Montagna, M.; Ronchin, S.; Tosello, C.; Ferrari, M. Metal Nanocluster Formation in Silica Films Prepared by rf-sputtering: An Experimental Study. *Eur. Phys. J. B* **2002**, *25*, 11−17.
(30) Shelemin, A.; Pleskunov, P.; Kousal, J.; Drewes, J.; Hanuš, J.; Ali-Ogly, S.; Nikitin, D.; Solař, P.; Kratochvíl, J.; Vaidulych, M.; Schwartzkopf, M.; Kylián, O.; Polonskyi, O.; Strunskus, T.; Faupel, F.; Roth, S. V.; Biederman, H.; Choukourov, A. Nucleation and Growth of Magnetron-Sputtered Ag Nanoparticles as Witnessed by Time-Resolved Small Angle X-Ray Scattering. *Part. Part. Syst. Charact.* **2020**, *37*, 1900436.
(31) Kousal, J.; Shelemin, A.; Schwartzkopf, M.; Polonskyi, O.; Hanuš, J.; Solař, P.; Vaidulych, M.; Nikitin, D.; Pleskunov, P.; Krtouš, Z.; Strunskus, T.; Faupel, F.; Roth, S. V.; Biederman, H.; Choukourov, A. Magnetron-Sputtered Copper Nanoparticles: Lost in Gas Aggregation and Found by in Situ X-Ray Scattering. *Nanoscale* **2018**, *10*, 18275−18281.
(32) Zhang, N.; Chen, F.; Wu, X.; Wang, Q.; Qaseem, A.; Xia, Z. The Activity Origin of Core-Shell and Alloy AgCu Bimetallic Nanoparticles for the Oxygen Reduction Reaction. *J. Mater. Chem. A* **2017**, *5*, 7043−7054.
(33) Kumar, M. K.; Bhavani, K.; Naresh, G.; Srinivas, B.; Venugopal, A. Plasmonic Resonance Nature of Ag-Cu/TiO2 Photocatalyst under Solar and Artificial Light: Synthesis, Characterization and Evaluation of H2O Splitting Activity. *Appl. Catal., B* **2016**, *199*, 282−291.
(34) Schuller, J. A.; Barnard, E. S.; Cai, W.; Jun, Y. C.; White, J. S.; Brongersma, M. L. Plasmonics for Extreme Light Concentration and Manipulation. *Nat. Mater.* **2010**, *9*, 193−204.
(35) Brown, M. D.; Suteewong, T.; Kumar, R. S. S.; D'Innocenzo, V.; Petrozza, A.; Lee, M. M.; Wiesner, U.; Snaith, H. J. Plasmonic Dye-Sensitized Solar Cells Using Core−Shell Metal−Insulator Nanoparticles. *Nano Lett.* **2011**, *11*, 438−445.
(36) Wang, J.-J.; Chen, C.; Chen, W.-G.; Yao, J.-S.; Yang, J.-N.; Wang, K.-H.; Yin, Y.-C.; Yao, M.-M.; Feng, L.-Z.; Ma, C.; Fan, F.-J.; Yao, H.-B. Highly Luminescent Copper Iodide Cluster Based Inks with Photoluminescence Quantum Efficiency Exceeding 98%. *J. Am. Chem. Soc.* **2020**, *142*, 3686−3690.
(37) Dong, B.; Yuan, Y.; Ding, M.; Bai, W.; Wu, S.; Ji, Z. Efficient Dual-Mode Luminescence from Lanthanide-Doped Core−Shell

nanoarchitecture for anti-counterfeiting applications. *Nanotechnology* **2020**, *31*, 365705.
(38) Liu, S.; Tian, X.; Guo, J.; Kong, X.; Xu, L.; Yu, Q.; Wang, A. X. Multi-Functional Plasmonic Fabrics: A Flexible SERS Substrate and Anti-Counterfeiting Security Labels with Tunable Encoding Information. *Appl. Surf. Sci.* **2021**, *567*, 150861.
(39) Dobrowolski, J. A.; Baird, K. M.; Carman, P. D.; Waldorf, A. Optical Interference Coatings for Inhibiting of Counterfeiting. *Opt. Acta* **1973**, *20*, 925−937.
(40) Kang, X.; Li, Y.; Zhu, M.; Jin, R. Atomically Precise Alloy Nanoclusters: Syntheses, Structures, and Properties. *Chem. Soc. Rev.* **2020**, *49*, 6443−6514.
(41) Beyene, H. T.; Chakravadhanula, V. S. K.; Hanisch, C.; Strunskus, T.; Zaporojtchenko, V.; Elbahri, M.; Faupel, F. Vapor Phase Deposition, Structure, and Plasmonic Properties of Polymer-Based Composites Containing Ag-Cu Bimetallic Nanoparticles. *Plasmonics* **2012**, *7*, 107−114.
(42) Vayalil, S. K.; Koorikkat, A.; Gopi, A. K.; Roth, S. V.; Kumar, P. S. A. Tailoring of Uniaxial Magnetic Anisotropy in Permalloy Thin Films Using Nanorippled Si Substrates. *J. Phys.: Condens. Matter* **2020**, *32*, 185804.
(43) Migliorini, L.; Piazzoni, C.; Pohako-Esko, K.; Di Girolamo, M.; Vitaloni, A.; Borghi, F.; Santaniello, T.; Aabloo, A.; Milani, P. All-Printed Green Micro-Supercapacitors Based on a Natural-derived Ionic Liquid for Flexible Transient Electronics. *Adv. Funct. Mater.* **2021**, *31*, 2102180.
(44) Barcaro, G.; Fortunelli, A.; Rossi, G.; Nita, F.; Ferrando, R. Electronic and Structural Shell Closure in AgCu and AuCu Nanoclusters. *J. Phys. Chem. B* **2006**, *110*, 23197−23203.
(45) Bao, Y.; Wu, X.; Gao, H.; Zhou, M.; Chen, S.; Jin, S.; Yu, H.; Zhu, M. The Geometric and Electronic Structures of a Ag13Cu10-(SAdm)12X3nanocluster. *Dalton Trans.* **2020**, *49*, 17164−17168.
(46) Abraham, J. W.; Bonitz, M. Molecular Dynamics Simulation of Ag−Cu Cluster Growth on a Thin Polymer Film. *Contrib. Plasma Phys.* **2018**, *58*, 164−173.
(47) Baletto, F.; Mottet, C.; Ferrando, R. Time Evolution of Ag-Cu and Ag-Pd Core-Shell Nanoclusters. *Eur. Phys. J. D* **2003**, *24*, 233−236.
(48) Radnóczi, G.; Bokányi, E.; Erdélyi, Z.; Misják, F. Size Dependent Spinodal Decomposition in Cu-Ag Nanoparticles. *Acta Mater.* **2017**, *123*, 82−89.
(49) Lü, B.; Souqui, L.; Elofsson, V.; Sarakinos, K. Scaling of Elongation Transition Thickness during Thin-Film Growth on Weakly Interacting Substrates. *Appl. Phys. Lett.* **2017**, *111*, 084101.
(50) Lü, B.; Elofsson, V.; Münger, E. P.; Sarakinos, K. Dynamic Competition between Island Growth and Coalescence in Metal-on-Insulator Deposition. *Appl. Phys. Lett.* **2014**, *105*, 163107.
(51) Zhou, Y.; Zhao, G.; Bian, J.; Tian, X.; Cheng, X.; Wang, H.; Chen, H. Multiplexed SERS Barcodes for Anti-Counterfeiting. *ACS Appl. Mater. Interfaces* **2020**, *12*, 28532−28538.
(52) Gensch, M.; Schwartzkopf, M.; Brett, C. J.; Schaper, S. J.; Kreuzer, L. P.; Li, N.; Chen, W.; Liang, S.; Drewes, J.; Polonskyi, O.; Strunskus, T.; Faupel, F.; Müller-Buschbaum, P.; Roth, S. V. Selective Silver Nanocluster Metallization on Conjugated Diblock Copolymer Templates for Sensing and Photovoltaic Applications. *ACS Appl. Nano Mater.* **2021**, *4*, 4245−4255.
(53) Schwartzkopf, M.; Hinz, A.; Polonskyi, O.; Strunskus, T.; Löhrer, F. C.; Körstgens, V.; Müller-Buschbaum, P.; Faupel, F.; Roth, S. V. Role of Sputter Deposition Rate in Tailoring Nanogranular Gold Structures on Polymer Surfaces. *ACS Appl. Mater. Interfaces* **2017**, *9*, 5629−5637.
(54) Greene, J. E. Review Article: Tracing the Recorded History of Thin-Film Sputter Deposition: From the 1800s to 2017. *J. Vac. Sci. Technol., A* **2017**, *35*, 05C204.
(55) Walter, H.; Bauer, G.; Domnick, R.; Jakopic, G.; Leitner, A. Role of Granular Structure in Metal Layers on the Optical Properties of Absorbing Mirrors. *Opt. Eng.* **2006**, *45*, 103801.
(56) Vegard, L. Die Konstitution der Mischkristalle und die Raumfüllung der Atome. *Z. Phys.* **1921**, *5*, 17−26.
(57) Jeffers, G.; Dubson, M. A.; Duxbury, P. M. Island-to-Percolation Transition during Growth of Metal Films. *J. Appl. Phys.* **1994**, *75*, 5016.
(58) Chen, H.; Zuo, J. Structure and Phase Separation of Ag-Cu Alloy Thin Films. *Acta Mater.* **2007**, *55*, 1617−1628.
(59) Schwartzkopf, M.; Buffet, A.; Körstgens, V.; Metwalli, E.; Schlage, K.; Benecke, G.; Perlich, J.; Rawolle, M.; Rothkirch, A.; Heidmann, B.; Herzog, G.; Müller-Buschbaum, P.; Röhlsberger, R.; Gehrke, R.; Stribeck, N.; Roth, S. V. From Atoms to Layers: In Situ Gold Cluster Growth Kinetics during Sputter Deposition. *Nanoscale* **2013**, *5*, 5053−5062.
(60) Schaper, S. J.; Löhrer, F. C.; Xia, S.; Geiger, C.; Schwartzkopf, M.; Pandit, P.; Rubeck, J.; Fricke, B.; Frenzke, S.; Hinz, A. M.; Carstens, N.; Polonskyi, O.; Strunskus, T.; Faupel, F.; Roth, S. V.; Müller-Buschbaum, P. Revealing the Growth of Copper on Polystyrene- Block-Poly(Ethylene Oxide) Diblock Copolymer Thin Films with in Situ GISAXS. *Nanoscale* **2021**, *13*, 10555−10565.
(61) Schwartzkopf, M.; Santoro, G.; Brett, C. J.; Rothkirch, A.; Polonskyi, O.; Hinz, A.; Metwalli, E.; Yao, Y.; Strunskus, T.; Faupel, F.; Müller-Buschbaum, P.; Roth, S. V. Real-Time Monitoring of Morphology and Optical Properties during Sputter Deposition for Tailoring Metal−Polymer Interfaces. *ACS Appl. Mater. Interfaces* **2015**, *7*, 13547−13556.
(62) Gensch, M.; Schwartzkopf, M.; Ohm, W.; Brett, C. J.; Pandit, P.; Vayalil, S. K.; Bießmann, L.; Kreuzer, L. P.; Drewes, J.; Polonskyi, O.; Strunskus, T.; Faupel, F.; Stierle, A.; Müller-Buschbaum, P.; Roth, S. V. Correlating Nanostructure, Optical and Electronic Properties of Nanogranular Silver Layers during Polymer-Template-Assisted Sputter Deposition. *ACS Appl. Mater. Interfaces* **2019**, *11*, 29416−29426.
(63) Kaune, G.; Ruderer, M. A.; Metwalli, E.; Wang, W.; Couet, S.; Schlage, K.; Röhlsberger, R.; Roth, S. V.; Müller-Buschbaum, P. In Situ GISAXS Study of Gold Film Growth on Conducting Polymer Films. *ACS Appl. Mater. Interfaces* **2009**, *1*, 353−360.
(64) Zaporojtchenko, V.; Strunskus, T.; Behnke, K.; Von Bechtolsheim, C.; Kiene, M.; Faupel, F. Metal/Polymer Interfaces with Designed Morphologies. *J. Adhes. Sci. Technol.* **2000**, *14*, 467−490.
(65) Fèvre, M.; Le Bouar, Y.; Finel, A. Thermodynamics of Phase-Separating Nanoalloys: Single Particles and Particle Assemblies. *Phys. Rev. B* **2018**, *97*, 195404.
(66) Grammatikopoulos, P.; Kioseoglou, J.; Galea, A.; Vernieres, J.; Benelmekki, M.; Diaz, R. E.; Sowwan, M. Kinetic Trapping through Coalescence and the Formation of Patterned Ag−Cu Nanoparticles. *Nanoscale* **2016**, *8*, 9780−9790.
(67) Chandross, M. Energetics of the Formation of Cu-Ag Core-Shell Nanoparticles. *Modell. Simul. Mater. Sci. Eng.* **2014**, *22*, 075012.
(68) Yang, H.; Wang, Y.; Chen, X.; Zhao, X.; Gu, L.; Huang, H.; Yan, J.; Xu, C.; Li, G.; Wu, J.; Edwards, A. J.; Dittrich, B.; Tang, Z.; Wang, D.; Lehtovaara, L.; Häkkinen, H.; Zheng, N. Plasmonic Twinned Silver Nanoparticles with Molecular Precision. *Nat. Commun.* **2016**, *7*, 12809.
(69) Raza, S.; Kadkhodazadeh, S.; Christensen, T.; Di Vece, M.; Wubs, M.; Mortensen, N. A.; Stenger, N. Multipole Plasmons and Their Disappearance in Few-Nanometre Silver Nanoparticles. *Nat. Commun.* **2015**, *6*, 8788.
(70) Luther, J. M.; Jain, P. K.; Ewers, T.; Alivisatos, A. P. Localized Surface Plasmon Resonances Arising from Free Carriers in Doped Quantum Dots. *Nat. Mater.* **2011**, *10*, 361−366.
(71) Yu, H.; Peng, Y.; Yang, Y.; Li, Z.-Y. Plasmon-Enhanced Light−Matter Interactions and Applications. *npj Comput. Mater.* **2019**, *5*, 45.
(72) Kim, S. H.; Kim, M.; Lee, J. H.; Lee, S.-J. Self-Cleaning Transparent Heat Mirror with a Plasma Polymer Fluorocarbon Thin Film Fabricated by a Continuous Roll-to-Roll Sputtering Process. *ACS Appl. Mater. Interfaces* **2018**, *10*, 10454−10460.
(73) Revenant, C. Anomalous Grazing-Incidence Small-Angle X-Ray Scattering of Ga2O3 -Based Nanoparticles. *J. Appl. Crystallogr.* **2018**, *51*, 436−445.

https://doi.org/10.1021/acsanm.1c04473
ACS Appl. Nano Mater. 2022, 5, 3832−3842